Materials Advances

ROYAL SOCIETY OF CHEMISTRY

PAPER

View Article Online
View Journal | View Issue

Cite this: *Mater. Adv.*, 2025, **6**, 8400

Multimodal luminescence and energy transfer mechanism in a narrowband UVB emitting phosphor system towards futuristic phototherapeutic devices

Aachal A. Sharma, Payal P. Pradhan, K. A. K. Durga Prasad, M. Rakshita, Raju Pembarthi and D. Haranath *

This investigation presents the synthesis and advanced spectroscopic characterization of Gd^{3+}-activated $CaMgSi_2O_6$ phosphors, synthesized *via* a high-temperature modified solid-state reaction method, tailored for narrowband ultraviolet B (UVB) phototherapeutic applications. The strategic incorporation of Gd^{3+} ions into the $CaMgSi_2O_6$ host lattice yields intense, sharp emission at 314 nm, attributed to the $^6P_{7/2} \rightarrow {}^8S_{7/2}$ intra-configurational transition under 275 nm excitation. Photoluminescence (PL) studies reveal five distinct 4f–4f and 4f–5d transitions, with the optimized composition, $Ca_{0.95}MgSi_2O_6$:$0.05Gd^{3+}$, demonstrating superior emission intensity ideal for treating dermatological conditions such as psoriasis. X-ray diffraction (XRD) analysis confirms a monoclinic crystal structure (space group *C*2/*c*), corroborated by alignment with the International Centre for Diffraction Data (ICDD, #01-075-0945), validating successful Gd^{3+} integration into the host matrix. Field-emission scanning electron microscopy (FESEM) reveals refined surface morphologies, with average particle sizes of 0.433 μm (pure) and 0.36 μm (x = 0.05 mol). Fourier transform infrared (FTIR) spectroscopy verifies the structural integrity of the silicate matrix, while Diffuse reflectance spectroscopy (DRS) indicates a narrowed bandgap upon Gd^{3+} activation. Temperature-dependent PL (TDPL) and time-resolved PL (TRPL) analyses elucidate exceptional thermal stability and efficient radiative energy transfer dynamics, respectively. These attributes position Gd^{3+}-activated $CaMgSi_2O_6$ as a highly promising candidate for next-generation, precise, and portable phototherapy devices, advancing dermatological treatment efficacy.

Received 26th July 2025,
Accepted 28th September 2025

DOI: 10.1039/d5ma00810g

rsc.li/materials-advances

1. Introduction

The quest for advanced luminescent materials in phototherapeutic applications has gained significant momentum in recent years, driven by the increasing need for precise, non-invasive, and patient-centric treatments for chronic dermatological conditions such as psoriasis, vitiligo, and eczema. A range of phototherapeutic modalities is commercially available, each tailored to specific wavelengths determined by the disease type, patient body surface area, severity index, and safety considerations. These therapies employ diverse light and laser sources, including ultraviolet (UV), visible, and infrared (IR) wavelengths, each operating through distinct mechanisms of action, as outlined in Table 1. Among these, narrowband ultraviolet B (UVB) radiation, considered as a first-line treatment, spanning 311–315 nm, has demonstrated exceptional efficacy in modulating immune responses and enhancing DNA repair mechanisms in keratinocytes and T-cells, thereby alleviating inflammatory symptoms associated with autoimmune skin disorders.[1–3] In this context, phosphor-converted UVB light sources provide notable advantages over traditional excimer lasers and mercury-based fluorescent lamps, offering superior spectral selectivity, reduced thermal output, extended operational lifetimes, and enhanced design flexibility.[4,5]

Rare-earth (RE)-activated phosphors have emerged as promising candidates for such applications owing to their sharp emission lines, high quantum yields, long lifetimes, and resistance to thermal and chemical degradation.[11] Among various RE ions, trivalent gadolinium (Gd^{3+}) is particularly attractive for UVB emission due to its stable half-filled $4f^7$ electronic configuration, facilitating allowed $^6P_{7/2} \rightarrow {}^8S_{7/2}$ transitions centered around ~313 nm.[12] This intraconfigurational transition is minimally affected by the host environment, as the outer 5s and 5p orbitals shield the 4f electrons. Consequently, Gd^{3+} exhibits high resistance to non-radiative decay, making it an ideal activator ion for UV-emitting phosphors.[13] However, due

Luminescent Materials and Devices (LMD) Group, Department of Physics, National Institute of Technology Warangal, Hanumakonda 506004, Telangana, India. E-mail: haranath@nitw.ac.in; Fax: +91 870 245 9547; Tel: +91 995 810 1115

Table 1 Wavelengths used to treat various skin diseases and corresponding modalities

Type of light	Wavelength range (nm)	Modality	Efficacy	Skin conditions to be treated	Ref.
Phototherapy					
UV					
(1) Broadband (BB) UVB	200–280	Mercury, halogen lamps, light-emitting diodes (LEDs), lasers	Most effective form of therapy. 90% patient skin rejuvenation.	Psoriasis, vitiligo, atopic dermatitis, pruritus, cutaneous T-cell lymphoma, *etc.*	6
(2) Narrowband UVB	311–315				
(3) PUVA (Psoralene + UVA)	320–400				
(4) Excimer laser	308				
Visible					
(1) Blue	400–495	LEDs, lasers, mask	Some benefits have been reported in a few reports.	Hyperbilirubinemia, hyperpigmentation, melasma, psoriasis, wound healing, acne, scarring, anti-aging, *etc.*	7 and 8
(2) Green	495–570				
(3) Yellow	570–590				
(4) Orange	590–620				
(5) Red	620–750		30–50% patient skin rejuvenation.		
(6) Pulsed dye laser	585–595				
(7) Intense pulsed laser	550–950				
IR					
(1) Near IR	750–950	LEDs	60–70%	Psoriasis, wound healing, scar reduction, skin conditioning.	9
(2) Nd:YAG laser	1064				
Combinational therapy					
(1) Photodynamic therapy (Photosensitizer activated by light)	600–850	Mercury, halogen lamps, LEDs	–	Actinic keratosis, basal cell carcinoma, acne, Bowen's disease, psoriasis.	10
(2) PUVB (Psoralene + UVB)	311–315				
(3) BB-UVB	290–320				
(4) Sunbath	400–760				

to the parity-forbidden nature of f–f transitions, direct excitation of Gd^{3+} is often inefficient. Therefore, careful selection of host lattices that can enhance energy transfer to Gd^{3+} through appropriate crystal field interactions and phonon dynamics is essential to achieve efficient UV-luminescence.[14]

Silicate-based hosts, particularly $CaMgSi_2O_6$ (diopside), present distinct advantages for luminescent applications. Diopside, a calcium-magnesium silicate within the monoclinic clinopyroxene family, is distinguished by its robust crystalline structure, exceptional thermal and chemical stability, and excellent biocompatibility.[15] Its adaptable lattice accommodates a diverse array of RE activators with minimal lattice strain, ensuring structural integrity and facilitating efficient substitution at Ca^{2+} sites.[16] Additionally, the three-dimensional silicate framework promotes efficient phonon-assisted energy transfer, enhancing the sensitization of RE ions such as Gd^{3+}. Ling *et al.* explored the incorporation of various activators into alkaline earth silicate matrices, elucidating their luminescence properties.[17,18] Furthermore, Kim *et al.*'s phase transformation studies on natural and synthetic diopside underscored its potential across diverse applications.[19] Owing to these attributes, silicate-based phosphors have garnered significant attention for use in solid-state lighting, bioimaging, and biomedical implants.[20,21]

The photoluminescence (PL) characteristics of Gd^{3+}-activated materials have been investigated in several host matrices. For instance, Ilya *et al.* reported efficient UVB emission at 313 nm in Gd^{3+}-activated $NaYF_4$ phosphors, with enhancements observed upon co-doping with Eu^{3+}.[22] Surender Kumar *et al.* synthesized Gd^{3+}-activated ZnO nanostructures exhibiting broad visible emission centered around 418 nm, demonstrating their utility in photocatalysis.[23] Dubey *et al.* studied Gd^{3+}-activated Y_2O_3 phosphors under 254 nm excitation and reported red emission at 613 nm due to energy migration pathways involving defect states.[24] The reports on Gd^{3+} activation in the KYF_4 matrix show that its luminescence, which arises from f–f transitions, is insensitive to the structural changes. Additionally, Park *et al.* demonstrated improved charge transport and energy level alignment in perovskite solar cells using Gd^{3+}-activated SnO_2 electron transport layers.[25] These findings highlight the multifunctionality of Gd^{3+} as an optical and electronic modifier, although its direct utility for UVB emission in silicate hosts remains inadequately explored.

The landscape of phototherapy is rapidly evolving toward compact, wearable, and patient-centered solutions. Recent innovations include flexible phototherapeutic patches or bandages that incorporate phosphor particles within polymeric matrices, allowing localized and controlled UVB irradiation.[26] Such innovative devices offer increased comfort, enable at-home treatment, and reduce side effects such as erythema and photodamage by delivering narrowly confined therapeutic wavelengths.[27] Incorporating Gd^{3+}-activated UVB phosphors into the polymeric systems holds the potential to enhance clinical outcomes, particularly in the treatment of psoriasis, where narrowband UVB is considered a customary standard.[28]

In this study, we report the synthesis and spectroscopic characterization of $Ca_{1-x}MgSi_2O_6{:}xGd^{3+}$ ($0.00 \leq x \leq 0.10$ mol)

phosphors synthesized *via* a modified solid-state reaction method. The emphasis is laid on optimizing the Gd^{3+} concentration for optimum UVB emission intensity, evaluating host–activator interactions, and elucidating the underlying energy transfer mechanisms through photoluminescence excitation (PLE), PL emission, temperature-dependent PL (TDPL) spectroscopy, and time-resolved PL (TRPL) spectroscopy. Additionally, the work shows a pathway for designing personalized, portable phototherapeutic devices.

2. Experimental section

2.1. Synthesis of the phosphor

The $Ca_{1-x}MgSi_2O_6{:}xGd^{3+}$ phosphor series (x = 0, 0.02, 0.05, 0.07, and 0.10 mol) was synthesized *via* a high-temperature modified solid-state reaction, a cost-effective and reproducible method. High-purity precursors such as CaO (99.99%), MgO (99.99%), SiO_2 (99.99%), and Gd_2O_3 (99.99%) were used without further purification. The reaction is represented as:

$$4CaO + 4MgO + 8SiO_2 + 2Gd_2O_3 \rightarrow 4CaMgSi_2O_6{:}xGd^{3+} + 3O_2\uparrow \quad (1)$$

Stoichiometric amounts of precursors were weighed, with CaO adjusted based on Gd^{3+} concentration due to the substitution of Gd^{3+} (ionic radius: 1.05 Å) for Ca^{2+} (1.12 Å). The mixture was ground in an agate mortar for 60 minutes to ensure homogeneity and then transferred to an alumina boat. As represented in Fig. 1, sintering was performed in a tubular furnace at 1300 °C for 180 minutes (heating rate: 5.42 °C min^{-1}) under an air atmosphere. After reaching room temperature, the resulting white powder was ground and stored for characterization.

2.2. Characterization

The synthesized phosphors were characterized using multiple techniques. Phase purity was confirmed using a Panalytical X-Pert powder diffractometer with CuKα radiation (λ = 1.5406 Å) over a 2θ range of 20–80°. Ultraviolet-visible (UV-Vis) diffuse reflectance spectroscopy (Analytik Jena Specord 210 Plus, 200–1200 nm) was used to determine absorption and band gap properties. Fourier Transform Infrared (FTIR) spectroscopy (Bruker Alpha-II) was conducted on 2 mm thick pellets (phosphor : KBr ratio = 1 : 9) in transmission mode (400–4000 cm^{-1}, 2 cm^{-1} resolution, 6 scans) to analyze vibrational modes. Photoluminescence (PL) excitation and emission spectra were recorded using a Hitachi F-4700 fluorescence spectrophotometer (200–900 nm). Temperature-dependent PL (TDPL) and time-resolved PL (TRPL) measurements were performed on a Horiba Fluorolog-3 spectrofluorometer to assess thermal stability and decay dynamics. All measurements were conducted at room temperature (25 °C) unless specified.

3. Results and discussion

3.1. Structural and morphological characterization

The XRD patterns shown in Fig. 2(a) confirmed the monoclinic structure (space group $C2/c$) of $Ca_{1-x}MgSi_2O_6{:}xGd^{3+}$ with x = 0, 0.02, 0.05, 0.07, and 0.10 mol, with lattice parameters a = 9.7100 Å, b = 8.8900 Å, c = 5.2400 Å, and V = 435.17 $Å^3$. Minor impurity peaks of strontium oxide were observed but deemed negligible due to their low intensity. The incorporation of Gd^{3+} into Ca^{2+} sites induced a slight lattice strain, evidenced by a peak shift from 29.99° to 30.03°. The proposed crystalline structure of the optimized phosphor is shown in Fig. 2(b). It consists of chains of SiO_4 tetrahedra connected by calcium (Ca) and magnesium (Mg) sites. These chains are characteristics of the pyroxene group of minerals. Calcium and magnesium are present in cubic and octahedral sites in the corresponding matrix. Due to comparable ionic radii of Gd^{3+} (1.05 Å) and Ca^{2+} (1.12 Å) ions, it usually replaces the cubic site in the $CaMgSi_2O_6$ matrix.

For a detailed analysis of the XRD peaks, Rietveld refinement analysis was carried out for the main phase of the synthesized sample, as shown in Fig. S1.

FE-SEM micrographs shown in Fig. 2(c and d) reveal flaky, layered morphologies with non-uniform particle size, and accumulation is present in some regions of the micrograph. The accumulation obtained from the results in the micrographs is due to the tendency of particles of the material to achieve a lower energy state by reducing the superficial area. The average particle sizes obtained were 0.433 μm (pure) and 0.36 μm (x = 0.05 mol), represented in the inset of Fig. 2(c and d). The EDX spectrum shown in Fig. 2(e) confirmed the presence of Ca, Mg, Si, O, and Gd, aligning with the expected stoichiometry.

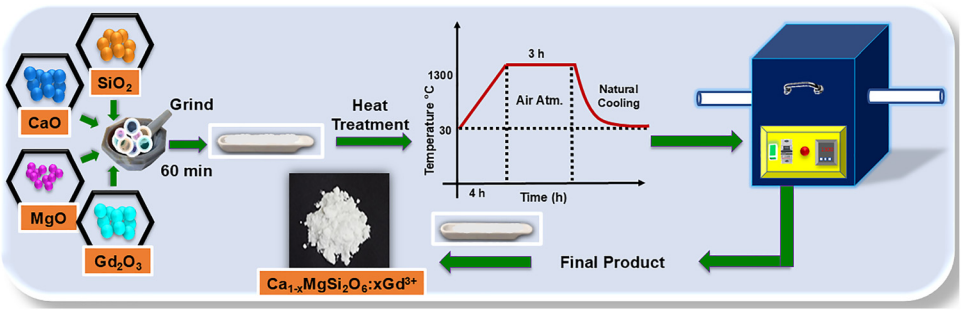

Fig. 1 High-temperature modified solid-state synthesis procedure of $Ca_{1-x}MgSi_2O_6{:}xGd^{3+}$ (x = 0, 0.02, 0.05, 0.07, and 0.10 mol).

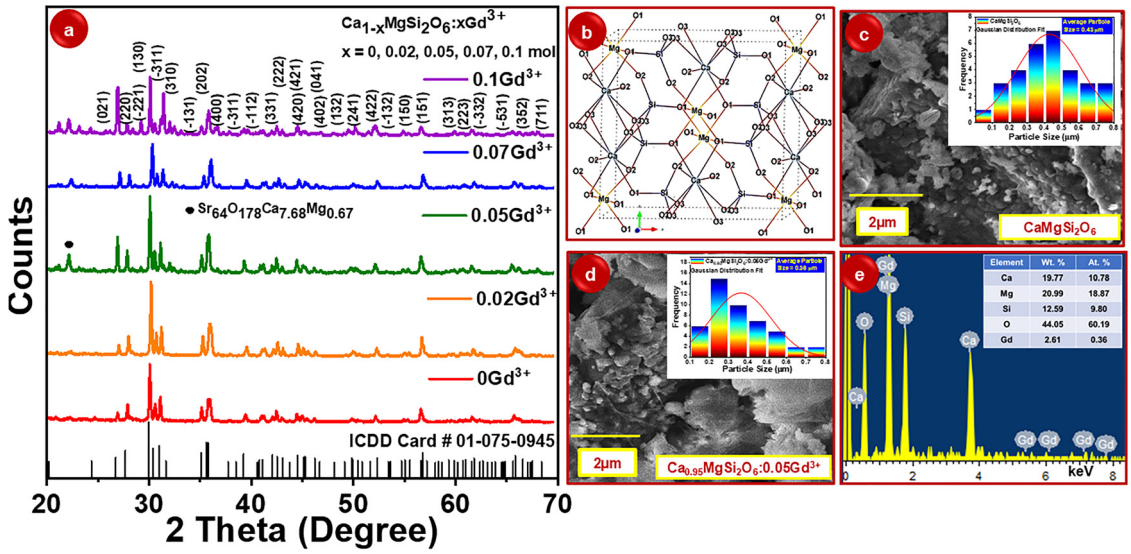

Fig. 2 (a) XRD patterns of $Ca_{1-x}MgSi_2O_6:xGd^{3+}$ phosphor series. (b) Crystallographic structure of the host matrix, (c) and (d) FE-SEM micrographs of the pure and optimum phosphor with the insets showing the average particle size plot, and (e) EDX data of the optimized $Ca_{0.95}MgSi_2O_6:0.05Gd^{3+}$ phosphor with atomic and weight percentage of its elements shown in inset table.

3.2. Diffuse reflectance spectroscopy (DRS) and optical band structure analysis

DRS is a powerful and non-destructive optical characterization technique employed to analyze both qualitative and quantitative aspects of the electronic and, in some cases, vibrational transitions in powder or polycrystalline materials.

It involves the irradiation of a sample with electromagnetic radiation in the UV-Visible-IR regions, followed by the measurement of diffusely reflected light intensity as a function of wavelength. The resulting spectrum reflects the electronic transitions and band structure features intrinsic to the material.[29] In the current investigation, DRS was employed to explore the optical absorption properties of the pure $CaMgSi_2O_6$ host and its Gd^{3+}-activated derivatives, as shown in Fig. 3(b and c). The DRS spectrum of the pure $CaMgSi_2O_6$ sample reveals strong absorption in the deep-to-far ultraviolet region (200–375 nm), while exhibiting minimal absorption in the visible range. This behavior confirms that the host matrix possesses a wide band gap suitable for activator ion emission, especially in the UVB region. The sample calcined at 1300 °C exhibited a sharp absorption edge at approximately 350 nm corresponding to a band gap of ~3.54 eV, shown in Fig. 3(a).

DRS spectra of Gd^{3+}-activated samples (x = 0.02, 0.05, 0.07, and 0.10 mol) show significant spectral evolution with increasing activator concentration. Fig. 3(a) reveals a prominent blue shift in the absorption edge, shrinking up to ~328 nm (3.78 eV) for the 0.05 mol Gd^{3+}-activated sample. The observed spectral shift is attributed to the introduction of intermediate electronic states within the band gap, coupled with enhanced photon absorption in the ultraviolet (UV) region. This phenomenon significantly improves the excitation efficiency of Gd^{3+} ions, enabling more effective energy transfer and luminescence performance.

The optical band gap (E_g) was determined using the Kubelka–Munk (K–M) function, which relates the diffuse reflectance (R) to the absorption coefficient *via* the equation:

$$F(R) = \frac{(1-R)^2}{2R} \quad (2)$$

The modified K–M function, suitable for indirect transitions, is plotted as $(F(R) \times h\nu)^{1/2}$ *versus* photon energy ($h\nu$). Extrapolation of the linear region to the photon energy axis yields the optical band gap. The estimated E_g values were 3.33 eV for the pure and 3.28 eV for the optimized Gd^{3+}-activated phosphor, indicating a slight narrowing of the band gap upon activator incorporation, shown in the inset of Fig. 3(b and c).

The observed modulation of the band gap arises from perturbations in the electronic structure induced by the substitutional incorporation of Gd^{3+} ions.[30] With its half-filled $4f^7$ configuration, Gd^{3+} features 4f orbitals shielded by $5d^1$ and $6s^2$ orbitals. As a result, 4f → 4f transitions are parity-forbidden and inherently weak, occurring primarily in the vacuum UV range (~170–200 nm). In contrast, 4f → 5d transitions are parity-allowed, facilitating robust absorption in the UV region. Furthermore, the integration of Gd^{3+} ions introduces defect states or localized distortions within the host matrix, which shift the absorption edge and enable photon absorption at lower energies. This structural and electronic interplay enhances the material's luminescence properties, underscoring its potential for advanced phototherapeutic applications.

Specific absorption transitions associated with Gd^{3+} ions were also evident in the absorption plot, as shown in Fig. 3(a). Transitions such as $^8S_{7/2} \rightarrow {}^6G_J$ (215–225 nm), $^8S_{7/2} \rightarrow {}^6D_J$ (238–260 nm), and $^8S_{7/2} \rightarrow {}^6I_J$ (260–280 nm; peak at 275 nm) were clearly resolved.[31,32] The pronounced absorption at 275 nm is particularly significant due to its alignment with excitation

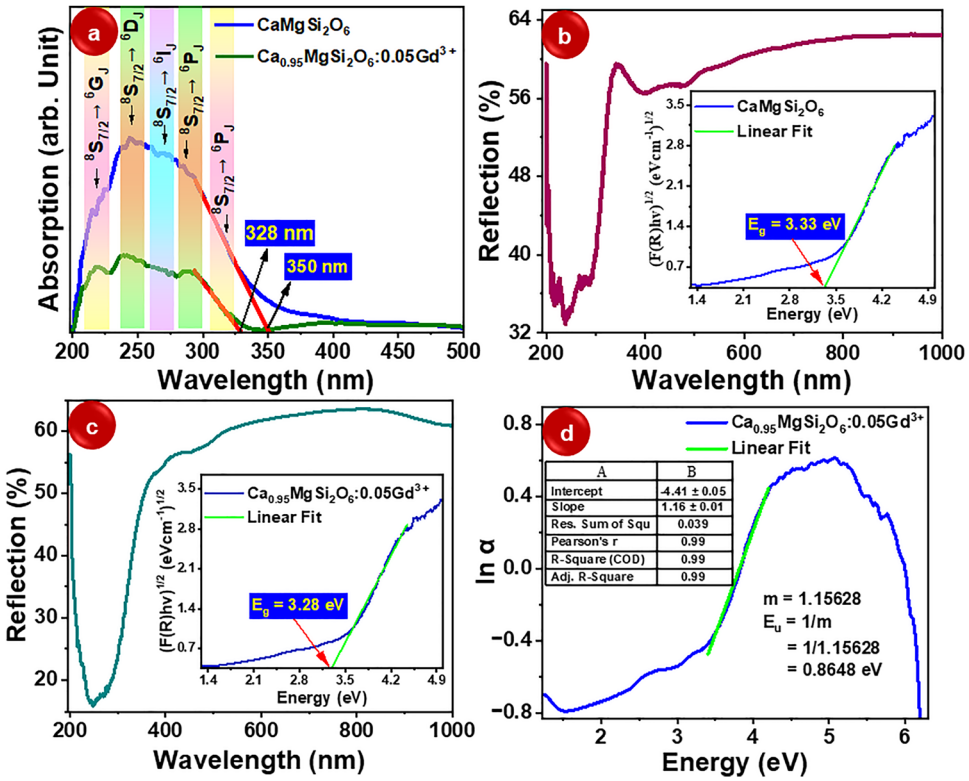

Fig. 3 (a) UV-Vis absorption spectrum of the $Ca_{1-x}MgSi_2O_6$:xGd^{3+} phosphor with x = 0 and x = 0.05 mol, representing the energy level transitions available for the emission. (b) and (c) Reflectance spectra with the Kubelka–Munk band gap energy calculations (inset). (d) Urbach energy plot and its energy parameters (inset) for the synthesized phosphor.

wavelengths commonly used for UV-pumped photonic applications, confirming efficient absorption and energy transfer in the optimized composition.

To evaluate the degree of structural disorder and the presence of defect states in the materials, Urbach energy (E_u) was calculated. The Urbach tail describes the exponential edge of the absorption band, which arises due to localized states in the band gap induced by structural disorder or thermal vibrations. The relationship between the absorption coefficient (α) and photon energy ($h\nu$) is given by:

$$\ln \alpha = \frac{h\nu}{E_u} - \frac{E_g}{E_u} + \ln \alpha_0 \quad (3)$$

This expression follows a linear form ($y = mx + c$), where the slope ($1/E_u$) is inversely proportional to the Urbach energy.[33] The plot of $\ln(\alpha)$ *vs.* $h\nu$ yields a straight line, from which the E_u value was extracted, as shown in Fig. 3(d). For the optimized $Ca_{0.95}MgSi_2O_6$:$0.05Gd^{3+}$ phosphor, the calculated Urbach energy was 0.8648 eV, indicating relatively low structural disorder and high crystallinity. A lower E_u value indicates a sharper absorption edge, reduced defect density, and improved structural ordering, all of which are critical factors for efficient PL performance.

The observed broad absorption profile with a significant tail toward lower photon energies further supports the existence of intermediate defect states or localized trap levels introduced due to Gd^{3+} activation. These defect states can play a vital role in non-radiative relaxation processes and affect the PL quantum yield. The controlled introduction of such states is essential for tuning emission intensity and decay dynamics in RE-activated phosphors.

As a whole, the DRS analysis confirms that Gd^{3+} ions are successfully incorporated into the $CaMgSi_2O_6$ lattice and influence the host's electronic structure by introducing intermediate states, narrowing the band gap, and enhancing UV absorption capability, an outcome highly desirable for UV-excitable phosphors for lighting and display technologies.[34]

3.3. Fourier transform infrared (FTIR) spectroscopic analysis

FTIR spectroscopy was employed to identify the functional groups and assess the local chemical environment of the synthesized $Ca_{1-x}MgSi_2O_6$:xGd^{3+} phosphor. FTIR is an indispensable vibrational spectroscopic technique that utilizes mid-infrared radiation (4000–400 cm^{-1}) to probe the vibrational modes of molecular bonds within a material. When the energy of incident IR photons matches the vibrational energy levels of specific chemical bonds, those bonds absorb the radiation, giving rise to characteristic absorption peaks. These peaks correspond to stretching, bending, and other vibrational transitions of functional groups, thus enabling qualitative and, in some cases, semi-quantitative chemical analysis.[35]

In this study, the FTIR spectra were recorded in the transmission mode over the spectral range of 4000–400 cm^{-1} with a resolution of 2 cm^{-1}. For optimal spectral acquisition,

pelletized samples were prepared by homogenizing the phosphor powder with spectroscopic-grade potassium bromide (KBr) in a 1 : 9 weight ratio and compressing the mixture into 2 mm thick translucent discs under vacuum.

The acquired spectra consist of two distinct regions I and II, *viz.* the functional group region (3700–1531 cm^{-1}), which primarily reveals surface-bound or residual organic and adsorbed species, and the fingerprint region (1300–400 cm^{-1}), which provides detailed information about the primary silicate framework and cation–oxygen coordination within the host lattice. The details of the two regions are described in the latter subsections.

3.3.1. Functional group region. In the functional group region, several identifiable vibrational bands were observed, as represented in Fig. 4. The broad absorption band around 3700 cm^{-1} is attributed to O–H stretching vibrations, indicative of surface-adsorbed moisture or hydroxyl species. The absorption band near 2927 cm^{-1} corresponds to the asymmetric stretching mode of aliphatic C–H groups, often originating from trace organic residues or environmental exposure during sample handling. A band at 2342 cm^{-1} is associated with the stretching vibration of atmospheric CO_2 (O═C═O), which may be adsorbed onto the surface or incorporated in minor quantities during sample preparation. The peak at 1722 cm^{-1} is assigned to C═O stretching vibrations, while the 1531 cm^{-1} peak is ascribed to asymmetric stretching of carboxylate (COO^-) groups, possibly originating from residual precursors or incomplete decomposition during synthesis. The presence of these bands indicates trace impurities or surface species that are typically eliminated upon high-temperature calcination but may persist in trace amounts due to chemisorption or kinetic trapping.[36]

3.3.2. Fingerprint region. The fingerprint region provides insights into the silicate lattice framework and metal–oxygen bonding in the $Ca_{1-x}MgSi_2O_6$:xGd^{3+} phosphors. As shown in Fig. 4, notable vibrational bands include the following: (i) a prominent peak at 1078 cm^{-1}, characteristic of Si–O–Si symmetric stretching vibrations within SiO_4 tetrahedra, where the bonds move in and out simultaneously relative to the central silicon atom.[37] (ii) A band at 855 cm^{-1}, attributed to Si–O asymmetric stretching modes. In this vibrational mode, one bond lengthens while the other shortens, typical of bridging oxygen atoms between adjacent SiO_4 tetrahedra. (iii) The 647 cm^{-1} band corresponds to O–Si–O bending vibrations, further confirming the integrity of the silicate network. Bending modes typically require lower excitation energies than stretching modes due to reduced bond stiffness. (iv) A weaker and broader band spanning the 518–460 cm^{-1} region is indicative of O–Mg–O non-bridging bending vibrations, which arise due to the localized distortion around the Mg^{2+} coordination environment. Interestingly, the expected vibrational feature associated with O–Ca–O bending modes, typically observed near 420 cm^{-1}, was absent or too weak to be resolved. This absence may be attributed to the relatively low content of CaO in the synthesized matrix or its partial substitution by Gd^{3+} ions.

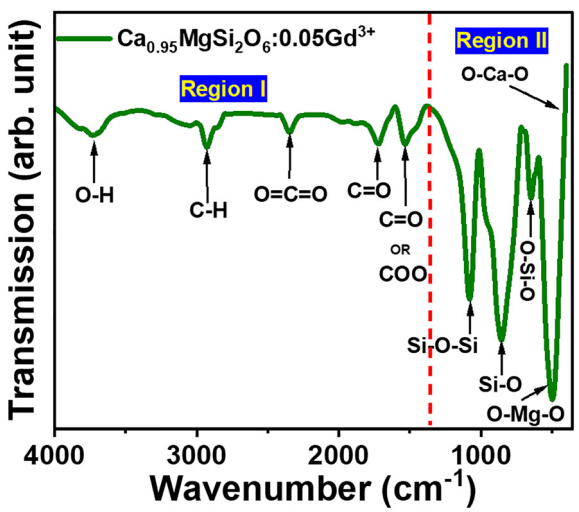

Fig. 4 FTIR data plot of the synthesized $Ca_{0.95}MgSi_2O_6$:$0.05Gd^{3+}$ phosphor.

3.3.3. Bonding environment and site occupation. The vibrational evidence suggests that Gd^{3+} ions in the diopside lattice may not occupy their typical tetrahedral sites but are instead stabilized in distorted or irregular cubic coordination due to the synthesis conditions. The Ca–O bonding is inferred to be predominantly covalent in nature, supported by the high covalency of bonds indicated by the absence of distinct ionic vibrations in the lower spectral region. Moreover, the substitution of Gd^{3+} for Ca^{2+} is structurally favorable due to their comparable ionic radii (Ca^{2+} = 1.12 Å; Gd^{3+} = 1.05 Å, both in 8-fold coordination) and is further facilitated by the similar charge balance and local coordination preferences. The lack of distortion-related bands or major shifts in the silicate framework peaks indicates that Gd^{3+} incorporation does not significantly disrupt the host lattice symmetry or connectivity.[38]

3.4. Luminescence studies

3.4.1. Photoluminescence excitation (PLE) spectroscopy. PLE spectroscopy is a powerful optical characterization tool that provides detailed insight into the electronic energy levels of luminescent materials, especially those with inherently weak absorption. It is particularly advantageous due to its superior signal-to-noise ratio compared to conventional absorption spectroscopy. PLE spectra are acquired by monitoring the emission intensity at a fixed wavelength while scanning a range of excitation wavelengths. The resulting spectral features correspond to the energy levels responsible for the excitation of valence electrons.

In the current study, the excitation spectra of the pure $CaMgSi_2O_6$ host were recorded by monitoring the emission at 332 nm, shown in Fig. 5(a). The excitation band extended from 245 to 300 nm, with a prominent maximum at 262 nm, indicating strong absorption in the UVC region (200–285 nm). This excitation facilitates photon emission in the UVA_2 region (320–340 nm), verifying that the host matrix possesses intrinsic self-luminescence properties in the near-UV region.

To improve excitation efficiency and explore potential UVB-emitting applications, the host matrix was activated with Gd^{3+}

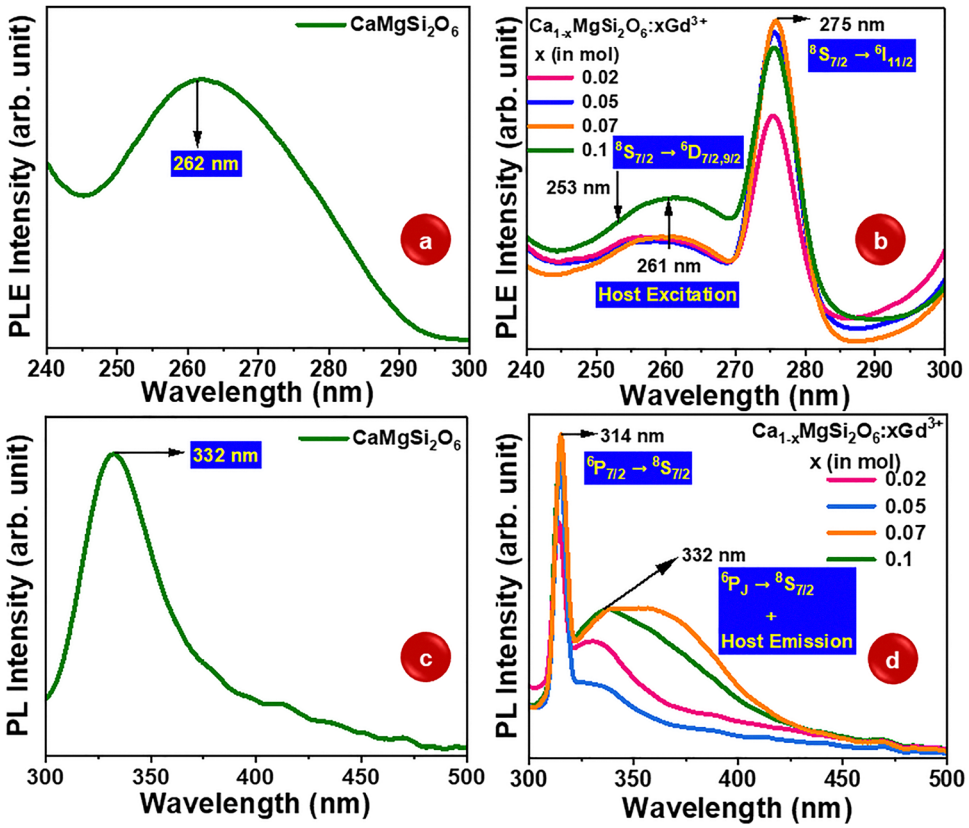

Fig. 5 (a) and (b) PLE and (c) and (d) PL plots of the pure (x = 0) and $Ca_{1-x}MgSi_2O_6$:xGd^{3+} (x = 0.02, 0.05, 0.07, and 0.10 mol) phosphor.

ions at varying concentrations (x = 0.02, 0.05, 0.07, and 0.10 mol). Fig. 5(b) reveals that upon Gd^{3+} incorporation, significant changes in the excitation spectra were observed. The PLE spectra for the Gd^{3+}-activated $CaMgSi_2O_6$ phosphor revealed two principal excitation bands, *viz.*, a broadband absorption extending from 240 to 270 nm with a maximum at 261 nm, attributed primarily to host-related charge transfer or band-to-band transitions, and a sharp and intense excitation peak centered at 275 nm, corresponding to the $^8S_{7/2} \rightarrow {}^6I_{11/2}$ transition of Gd^{3+} ions.

An additional shoulder at ~253 nm is associated with the ^6D_J excitation levels of Gd^{3+}, overlapping the host absorption band. Although the transition $^8S_{7/2} \rightarrow {}^6G_J$ (expected at ~202 nm) is allowed, its corresponding band was not observed, likely due to weak intensity and significant noise interference in the vacuum UV region.[39]

The onset of the excitation edge for both pure and Gd^{3+}-activated $CaMgSi_2O_6$ remained unchanged at 240 nm. However, the slight blue shift in the excitation maxima from 262 nm (pure) to 261 nm (Gd^{3+}-activated) implies a subtle alteration in the conduction band structure induced by Gd^{3+} substitution. The overlapping of the host and Gd^{3+} excitation bands suggests efficient energy transfer from the host lattice to the Gd^{3+} centers, effectively sensitizing the desired ^6I_J excited states.[40]

The narrow, intense, and well-defined peak at 275 nm (270–280 nm range) is directly attributed to Gd^{3+} ion excitation and is responsible for the dominant UVB emission at 314 nm. This 275 nm excitation was selected for subsequent PL emission studies, as the 261 nm band was found to yield a broader and less intense emission in the UVA_2 region.

3.4.2. Photoluminescence (PL) spectroscopy. PL spectroscopy probes the light-emitting behavior of materials upon excitation by an external photon source. It is a non-destructive, highly sensitive, and widely used technique for exploring luminescence mechanisms and defect-related emission in functional materials.[41]

PL measurements in Fig. 5(c) showed that excitation at 262 nm resulted in a broad and weak emission band centered at 332 nm, attributed to intrinsic luminescence from the host matrix. This weak band likely arises from defect-related states such as oxygen vacancies, cation site disorder (Ca^{2+} or Mg^{2+}), or non-stoichiometric deviations. Based on the PLE and DRS analyses, the optimized excitation wavelength of 275 nm was chosen to study the PL response of Gd^{3+}-activated $CaMgSi_2O_6$ phosphors. Under 275 nm excitation, the PL emission spectra exhibited an intense and narrow emission peak at 314 nm for varied activator concentration phosphors corresponding to the spin-allowed $^6P_{7/2} \rightarrow {}^8S_{7/2}$ transition of Gd^{3+} ions[42] as represented in Fig. 5(d).

The emission profile is characteristic of Gd^{3+} ions and confirms efficient energy transfer and radiative relaxation from the ^6P_J state. The full width at half maximum (FWHM) of the 314 nm emission was found to be 6.22 nm, indicating a sharp and spectrally pure transition, as shown in Fig. 6(a).

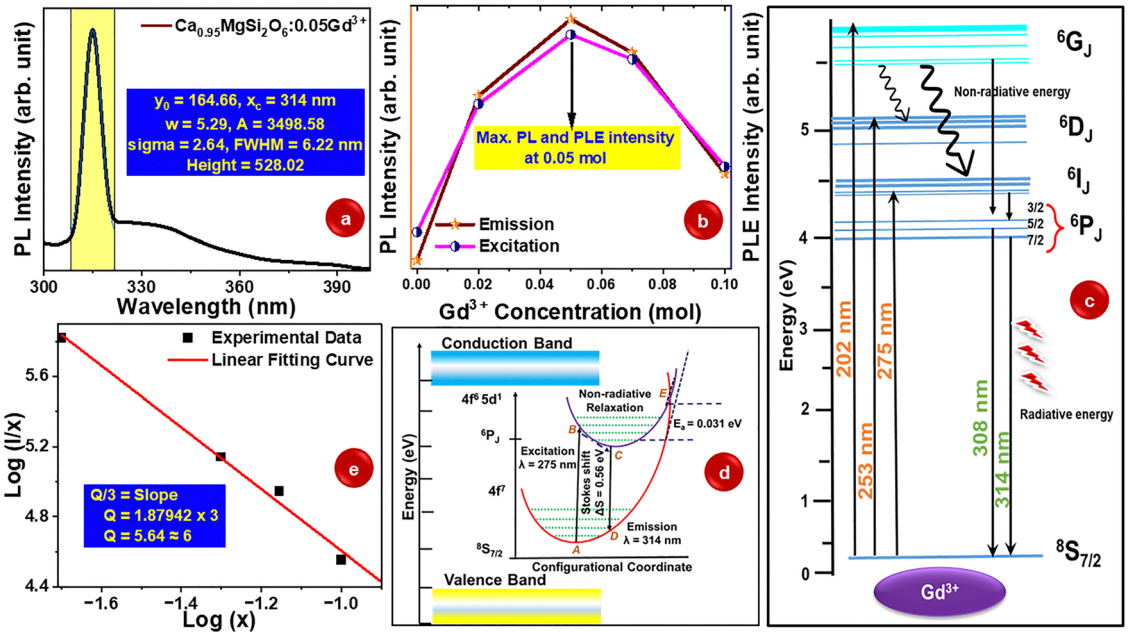

Fig. 6 (a) Plot shows the FWHM calculated value for optimized $Ca_{0.95}MgSi_2O_6$:0.05Gd^{3+} phosphor. (b) Variation in the PL and PLE intensity with the activator concentration. (c) Energy level diagram of Gd^{3+} transitions. (d) Configurational coordinate diagram of Gd^{3+}. (e) Non-radiative energy transfer analysis by using Van Uitert's study.

Such narrow emission bandwidths are indicative of a well-ordered lattice with minimal inhomogeneous broadening or defect-induced perturbations.

Upon increasing the Gd^{3+} concentration from x = 0.02 to 0.10 mol, the PL emission intensity at 314 nm first increased, reaching a maximum at x = 0.05, and then decreased beyond this optimum value plotted in Fig. 6(b). This behavior is attributed to concentration quenching, wherein non-radiative energy transfer mechanisms, such as cross-relaxation and energy migration to quenching sites, become dominant at higher activator concentrations.[43] Below the threshold ($x \leq$ 0.05), Gd^{3+} ions are well-separated, minimizing these non-radiative interactions and promoting efficient radiative transitions. Several potential Gd^{3+}-related transitions were examined based on reported energy level schemes, as shown in Fig. 6(c):

(i) $^6G_J \rightarrow {}^6I_J$ and $^6G_J \rightarrow {}^6D_J$ transitions are expected to emit in the IR region (~762 nm and ~1000 nm, respectively); however, these transitions were not detected in the current work due to their weak oscillator strengths and instrumental spectral limitations.

(ii) $^6G_J \rightarrow {}^8S_{7/2}$ transitions, emitting around 200 nm, require hosts transparent above ~50 000 cm^{-1} and were not supported by the chosen silicate matrix.

(iii) $^6P_J \rightarrow {}^8S_{7/2}$ transition at 314 nm was the most prominent and observable, consistent with literature reports for Gd^{3+}-activated phosphors.

The configurational coordinate diagram (CCD) for the Gd^{3+} ion, as represented in Fig. 6(d), is drawn to understand the Stokes shift phenomenon, absorption or emission band temperature dependency, and, most importantly, the thermal quenching phenomenon of the Gd^{3+} ion precisely.[44] The temperature-dependent behavior of Gd^{3+} ions, particularly the thermal quenching phenomenon, has been meticulously characterized. Under ultraviolet (UV) excitation, Gd^{3+} ions transition from the ground state, $^8S_{7/2}$, to the excited state, ^6P_J, as depicted by the A → B process. At the excited state (B), electrons lose a portion of their energy through lattice vibrations, relaxing non-radiatively to the equilibrium position (C). The subsequent radiative emission occurs *via* the C → D transition, followed by relaxation from D → A, returning to the ground state. The energy difference between the absorption and emission bands, known as the Stokes shift, is measured at 0.56 eV. As the temperature rises, electrons in the ^6P_J state gain sufficient thermal energy to cross the intersection point (E) in the CCD, returning to the ground state non-radiatively. This process, governed by the activation energy (E_g), results in the quenching of PL intensity. Moreover, elevated temperatures enhance electron–phonon coupling, altering the equilibrium positions of the excited and ground state potential energy curves. This modification induces a shift in emission toward both higher and lower wavelength regions, reflecting the dynamic interplay between thermal effects and luminescence properties.

Moreover, the overlapping of emission states between the host matrix (332 nm) and the activator (314 nm) adds an advantageous dual-luminescent characteristic to the phosphor, although the host emission is strongly quenched due to efficient Gd^{3+}-related processes. The substitution of Gd^{3+} at Ca^{2+} sites in the $CaMgSi_2O_6$ lattice is structurally feasible. This substitution necessitates charge compensation, which is presumably achieved *via* local activator clustering or formation of associated defect pairs. The presence of such clusters is supported by the enhanced PL intensity and optimized energy transfer efficiency observed at x = 0.05 Gd^{3+} concentration.[45]

Table 2 List of reported UVB-emitting phosphors

Sr. no.	Synthesis route	Name of the phosphor	Excitation	Emission	Ref.
1	Combustion synthesis	$CaYAl_3O_7:Gd^{3+}$	272	307, 313	46
2	Hydrothermal synthesis	$Li_4ZrF_8:Gd^{3+}$	273	312	47
3	Solid state synthesis	$Sr_3(PO_4)_2$:1%Gd^{3+}	273	311, 313	48
4	Co-precipitation method	$CaSO_4:Gd^{3+}$	275	313	49
5	**Solid-state synthesis**	**$CaMgSi_2O_6:Gd^{3+}$**	**274**	**314**	**This work**

The comparative study of the synthesized phosphor series with other reports is mentioned in Table 2.

3.4.3. Radiative and non-radiative energy transfer mechanisms. The energy transfer mechanism was elucidated by considering both radiative and non-radiative processes. In the case of radiative transfer, energy is emitted from the host matrix and subsequently reabsorbed by nearby Gd^{3+} ions. In contrast, non-radiative transfer occurs without photon emission, relying instead on Coulombic or exchange interactions.

To assess the influence of activator concentration on energy transfer, the critical distance (R_c) for Gd^{3+}–Gd^{3+} interactions was estimated using the Blasse equation:

$$R_c \approx 2\left(\frac{3V}{4\pi x_c N}\right)^{\frac{1}{3}} \quad (4)$$

where $V = 435.17$ Å^3 is the volume of the unit cell, $x_c = 0.05$ mol is the optimal Gd^{3+} concentration, and $N = 16$ is the number of cations per unit cell. Substituting these values yields a critical distance of $R_c = 10.13$ Å. When the average distance between activator ions falls below R_c, non-radiative energy transfer dominates, leading to luminescence quenching.

According to Dexter's theory,[50] non-radiative energy transfer occurs *via* three principal mechanisms, *viz.*, radiative reabsorption, exchange interaction, and electric multipolar interactions. Radiation reabsorption occurs when there is spectral overlap between the donor's emission and the acceptor's absorption. However, in the current system, no significant overlap between the excitation and emission spectra of Gd^{3+} was observed, ruling out radiation reabsorption. The exchange interaction mechanism involves the quantum mechanical exchange of electrons and becomes significant only when donor and acceptor wavefunctions overlap spatially. It operates efficiently at short distances (typically ≤ 5 Å). Given the calculated R_c (10.13 Å), exchange interactions are unlikely in this system. The electric multipolar interaction mechanism is dominant at distances > 5 Å and includes dipole–dipole, dipole–quadrupole, and quadrupole–quadrupole couplings. The nature of the multipolar interaction responsible for energy transfer and concentration quenching was analyzed using Van Uitert's formalism[51]:

$$\frac{I}{x} = k\left[1 + \beta(x)^{\frac{Q}{3}}\right]^{-1} \quad (5)$$

Taking the logarithm of both sides gives:

$$\log\left(\frac{I}{x}\right) = \log k - \frac{Q}{3}\log x \quad (6)$$

Plotting $\log\left(\frac{I}{x}\right)$ *vs.* $\log x$ in Fig. 6(e) yields a straight line with slope $-Q/3$. From the linear fit, the extracted value of Q was 5.64, closely approximating 6. This corresponds to a dipole–dipole interaction, confirming that the concentration quenching observed at a higher Gd^{3+} content arises primarily from electric dipole–dipole coupling between closely spaced activator ions. As the Gd^{3+} concentration increases, these interactions intensify, facilitating non-radiative transitions *via* cross-relaxation or phonon-assisted energy migration to killer centers.[52]

Furthermore, the substitution of trivalent Gd^{3+} ions into the divalent Ca^{2+} sites in the diopside matrix necessitates charge compensation. This is likely achieved *via* the formation of neutral clusters or associated defects, which may enhance or hinder the energy transfer depending on their spatial arrangement and interaction dynamics.

3.5. Temperature-dependent photoluminescence (TDPL) spectroscopy

TDPL spectroscopy is a powerful method for elucidating the fundamental optical and electronic behavior of phosphor materials as a function of temperature. This technique enables the assessment of carrier dynamics, exciton stability, energy transfer efficiency, phonon-assisted deactivation, and defect-related recombination mechanisms. With increasing temperature, thermal energy facilitates phonon-assisted processes that can dissociate excitons and enhance non-radiative recombination channels, thereby altering both the intensity and spectral position of PL emission.

The Gd^{3+}-activated $CaMgSi_2O_6$ phosphor series exhibited a strong PL emission peak centered at 314 nm under 275 nm excitation. To investigate the thermal stability, quenching behavior, and electron–phonon coupling effects of the optimized composition ($Ca_{0.95}MgSi_2O_6$:0.05Gd^{3+}), TDPL analysis was performed in the range of 20 °C to 80 °C, as shown in Fig. 7(a). Additionally, a minor spectral redshift of less than a nanometer was observed in the emission peak position as the temperature increased. The emission peak shifts were non-linear for temperature, suggesting complex thermally induced effects, including crystal lattice expansion or contraction and variations in crystal field strength. These effects modify the energy separation between the ^6P_J and ^8S_J levels of Gd^{3+}, thereby causing slight emission peak fluctuations. In silicate matrices, the splitting of degenerate energy levels due to thermally induced symmetry distortions can lead to observable shifts in the emission band, consistent with the observed behavior.

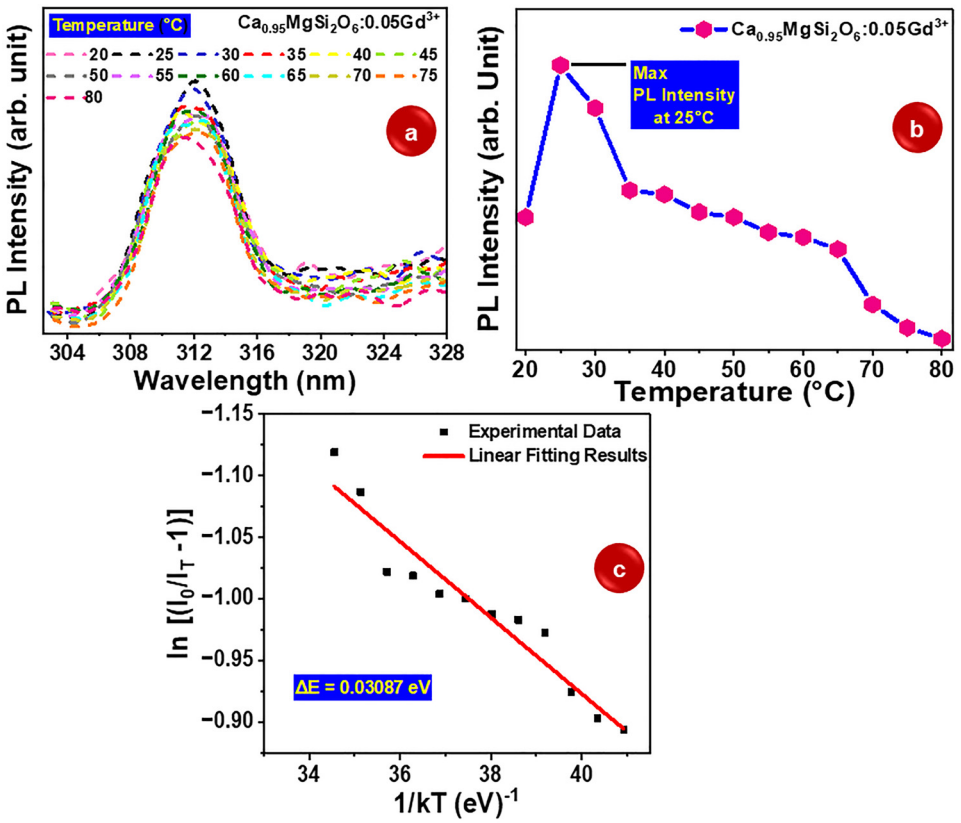

Fig. 7 (a) TDPL plot of optimized phosphor at different temperatures, (b) Variation of PL intensity with temperature, and (c) Activation energy determination by the linear fitting method using the Arrhenius equation.

In the current study, Fig. 7(b) shows that TDPL measurements of $Ca_{0.95}MgSi_2O_6:0.05Gd^{3+}$ revealed that the emission intensity increased slightly from room temperature up to ~25 °C and subsequently decreased monotonically with further temperature increase. The initial rise in intensity is often associated with the release of trapped carriers or thermally activated defect recombination, which temporarily enhances radiative recombination efficiency. However, at higher temperatures, increased lattice vibrations (phonon population) dominate, intensifying the probability of non-radiative transitions *via* multi-phonon relaxation or thermally activated quenching processes.[53] This leads to a reduction in the number of excited carriers available for radiative recombination and hence a progressive decline in PL intensity.

To quantitatively evaluate the thermal quenching behavior, the experimental PL intensity data as a function of temperature were analyzed using the modified Arrhenius model:

$$I_T = I_0\left[1 + c\exp\left(-\frac{\Delta E}{k_B T}\right)\right]^{-1} \quad (7)$$

where I_T denotes the integrated PL intensity at temperature T, I_0 is the PL intensity at the reference temperature (25 °C), ΔE is the thermal activation energy, c is a pre-exponential constant given by τ_R/τ_0 (where τ_R and τ_0 represent radiative and non-radiative lifetimes, respectively), k_B is the Boltzmann constant (8.629×10^{-5} eV K^{-1}), and T is the absolute temperature in Kelvin.

The linearized form of the equation, $\ln[(I_0/I_T) - 1] = (\Delta E/k_B T) + \ln c$, was used to construct a plot of $\ln[(I_0/I_T) - 1]$ *vs.* $1/k_B T$, as shown in Fig. 7(c). The slope of the fitted line corresponds to the thermal activation energy ΔE. The estimated activation energy from the fit was found to be 0.03087 eV, indicating moderate resistance to thermal quenching.[54] This relatively low value suggests that thermal energy ($\sim k_B T$) at elevated temperatures facilitates non-radiative relaxation, yet the emission retains appreciable intensity up to 80 °C, demonstrating its suitability for near-UV optoelectronic or phototherapy applications.[55]

The observed quenching pattern and the activation energy are in line with the behavior of other rare-earth-activated silicate phosphors, where the robust host lattice and the shielding of 4f electrons minimize the interaction of luminescent centers with phonons.[56] The silicate framework further contributes to structural rigidity and thermal stability, although complete suppression of quenching at elevated temperatures typically requires compositional or structural optimization (*e.g.*, host lattice modification or co-doping strategies).

3.6. Time-resolved photoluminescence (TRPL) analysis

To gain an in-depth understanding of the energy transfer dynamics and luminescence decay mechanisms in the synthesized

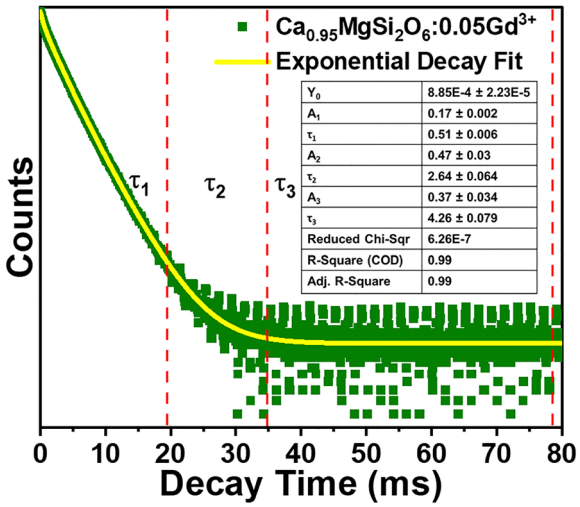

Fig. 8 Lifetime decay plot of the $Ca_{0.95}MgSi_2O_6{:}0.05Gd^{3+}$ phosphor fitted with the exponential fitting parameters represented in the inset.

$Ca_{1-x}MgSi_2O_6{:}xGd^{3+}$ phosphors, TRPL measurements were carried out on the optimized composition ($x = 0.05$ mol). The TRPL decay curve was recorded at an emission wavelength of 314 nm following excitation at 275 nm using a pulsed source with a chopping frequency of 10 Hz and an illumination duration of 60 seconds, as represented in Fig. 8. The decay profile reflects the relaxation behavior of the excited Gd^{3+} ions, specifically the $^6P_{7/2} \rightarrow {}^8S_{7/2}$ radiative transition.[57]

The decay curve exhibited a non-single exponential behavior, indicative of multiple luminescent centers or relaxation pathways. Hence, the experimental decay data were best fitted using a tri-exponential decay model, described using the following equation:

$$I(t) = I_0 + A_1 e^{\left(\frac{-t}{\tau_1}\right)} + A_2 e^{\left(\frac{-t}{\tau_2}\right)} + A_3 e^{\left(\frac{-t}{\tau_3}\right)} \quad (8)$$

where $I(t)$ and I_0 represent the emission intensities at time t and zero, respectively; A_1, A_2, and A_3 are amplitude constants corresponding to the fast, intermediate, and slow decay components; and τ_1, τ_2, and τ_3 are their respective lifetimes. The average lifetime τ_{avg} of the phosphor was calculated using the intensity-weighted mean lifetime formula:

$$\tau_{avg} = \frac{(A_1\tau_1^2 + A_2\tau_2^2 + A_3\tau_3^2)}{(A_1\tau_1 + A_2\tau_2 + A_3\tau_3)} \quad (9)$$

Substituting the fitted values yields an average lifetime of 3.45 ms, demonstrating long-lived emission behavior typically associated with forbidden transitions in Gd^{3+} ions.

4. Flexible devices for phototherapy using the narrowband UVB emitting phosphor

Narrowband UVB phototherapy is recognized as a highly effective, safe, and targeted approach among all other treatment modalities for the treatment of numerous dermatological conditions, including psoriasis, vitiligo, lichen sclerosus, atopic dermatitis, chronic pruritus, *etc.*[58,59] A wide array of phototherapeutic devices has been employed in clinical practice, including fluorescent lamps, fiber-optic systems, infrared lamps, excimer lasers, and phosphor-based LEDs.[60] However, the existing phototherapy instruments are large, bulky, non-flexible, and expensive, generate more heat, and require professional operation for the treatment. Also, patients need to go to the hospital every time due to longer cycle treatment, which affects their mental, physical, and economic health conditions badly. Therefore, it is of great significance to develop wearable and flexible phototherapeutic devices to facilitate patients' treatment in the community or at home. Such patient-centric, non-invasive treatment solutions are needed for a significant shift in the context of modern healthcare tools.[61] Limited literature on this ideology has created a significant interest in overcoming this research gap. In this research, we proposed an innovative and smart idea of wearable and flexible phosphor-based phototherapeutic devices for the treatment of skin diseases. In order to fabricate such a device, $Ca_{0.95}MgSi_2O_6{:}0.05Gd^{3+}$ phosphor can be blended with a polymer matrix such as polydimethylsiloxane (PDMS) or liquid silicone, which are known for their use in biomedical applications.[62] The proposed protocol for the development of flexible bandages/patches and smart bands is shown in the schematic of Fig. 9(a and b).

Furthermore, the smart band can also be integrated with a timer to adjust the dosage time and an intensity controller to prevent excessive exposure to UVB radiation. Additional features, such as real-time feedback, memory backup, and cloud integration for dermatologist monitoring, can also be accessed *via* the mobile app by integrating sensing features into the smart band.

The above-proposed flexible phototherapeutic devices can provide ergonomic application on curved or jointed anatomical regions, enhanced patient comfort, and self-administered use in decentralized or home-care environments. The lightweight design and ease of fabrication support scalability for broader clinical adaptation, particularly in resource-limited settings. With the integration of optimized rare-earth activated phosphors and flexible optoelectronic components, the proposed prototype aligns with the emerging paradigm of wearable, patient-centric, and intelligent phototherapy systems.[58,63,64] This approach not only ensures spectral precision but also

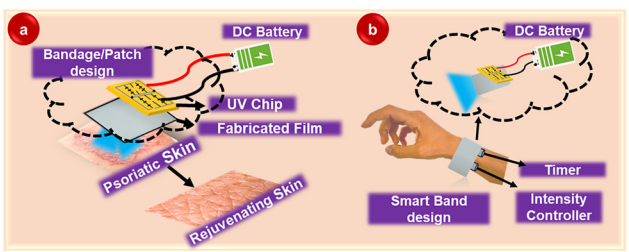

Fig. 9 Schematic diagram of the device fabrication protocol.

opens up new pathways for personalized, low-risk, and energy-efficient treatment strategies.

5. Conclusion

The Gd^{3+}-activated $CaMgSi_2O_6$ phosphors, synthesized *via* a solid-state reaction, demonstrated exceptional potential as narrowband UVB emitters for phototherapy. The optimized composition ($Ca_{0.95}MgSi_2O_6$:$0.05Gd^{3+}$) exhibited intense, narrow-band emission at 314 nm, driven by the $^6P_{7/2} \rightarrow {}^8S_{7/2}$ transition under 275 nm excitation. FTIR confirmed the silicate matrix's structural integrity, while DRS and PL analyses elucidated the electronic and luminescence properties. TDPL and TRPL studies highlighted the phosphor's thermal stability and efficient energy transfer, with a radiative lifetime of 3.45 ms. The proposed device fabrication protocol, which integrates the phosphor into flexible polymeric films, offers a practical pathway for developing portable, patient-centric phototherapy devices. These findings position Gd^{3+}-activated $CaMgSi_2O_6$ as a transformative material for dermatological treatments, paving the way for advanced, personalized healthcare solutions.

Author contributions

Aachal A. Sharma: data curation, methodology, investigation, formal analysis, writing paper, and editing. Payal P. Pradhan: data curation and formal analysis. K. A. K. Durga Prasad: data curation and formal analysis. M. Rakshita: data curation and formal analysis. R. Pembarthi: data curation and formal analysis. D. Haranath: conceptualization, funding acquisition, methodology, supervision, and writing – review & editing.

Conflicts of interest

The authors have no conflicts of interest to declare.

Data availability

The data that support the findings of this study are available from the corresponding author upon reasonable request.

Supplementary information (SI) is available. See DOI: https://doi.org/10.1039/d5ma00810g.

Acknowledgements

The authors AAS, MR, and DH are grateful to the Department of Science and Technology (DST) and Council of Scientific & Industrial Research (CSIR), Government of India, for providing financial support under various projects *viz* INSPIRE scheme #IF200233, CSIR-SRF #09/0922(11518)/2021-EMR-I, and #CRG/2021/007142, respectively.

References

1 T. Gambichler, F. Breuckmann, S. Boms, P. Altmeyer and A. Kreute, Narrowband UVB phototherapy in skin conditions beyond psoriasis, *J. Am. Acad. Dermatol.*, 2005, **52**, 660–670, DOI: 10.1016/j.jaad.2004.08.047.

2 S. Dogra and D. De, Narrowband ultraviolet B in the treatment of psoriasis: The journey so far!, *Indian J. Dermatol. Venereol.*, 2010, **76**, 652–661, DOI: 10.4103/0378-6323.72461.

3 J. A. Parrish and K. F. Jaenicke, Action Spectrum for Phototherapy of Psoriasis, *J. Invest. Dermatol.*, 1981, **76**, 359–362, DOI: 10.1111/1523-1747.ep12520022.

4 J. Muller, I. B. Ramsteiner, R. FieB and C. Neumann, High-radiance phosphor-converted light sources for fluorescence analysis, *Adv. Opt. Technol.*, 2024, **13**, 1510954, DOI: 10.3389/aot.2024.1510954.

5 P. Zdeb, N. Rebrova and P. J. Deren, Discovering the Potential of High Phonon Energy Hosts in the Field of Visible-to-Ultraviolet C Upconversion, *J. Phys. Chem. Lett.*, 2024, **15**(37), 9356–9360, DOI: 10.1021/acs.jpclett.4c02053.

6 P. S. Hemne, R. G. Kunghatkar, S. J. Dhoble, S. V. Moharil and V. Singh, Phosphor for phototherapy: Review on psoriasis, *Luminescence*, 2017, **32**(3), 260–270, DOI: 10.1002/bio.3266.

7 B. H. Mahmoud, C. L. Hexsel, I. H. Hamzavi and H. W. Lim, Effects of Visible Light on the Skin, *Photochem. Photobiol.*, 2008, **84**, 450–462, DOI: 10.1111/j.1751-1097.2007.00286.x.

8 A. Alexis, A. McMichael, J. Soung, O. Choi, T. Alkousakis, J. Alonso-Llamazares, M. Shahriari, A. O. Rodriguez, T. Bhutani, D. Chan and K. Rowland, Desai, Guselkumab for Moderate to Severe Psoriasis Across All Skin Tones Cohort A of the VISIBLE Randomized Clinical Trial, *JAMA Dermatol.*, 2025, e251836, DOI: 10.1001/jamadermatol.2025.1836.

9 J. Xia, L. Ding and G. Liu, Metabolic syndrome and dermatological diseases: association and treatment, *Nutr. Metab.*, 2025, **22**(1), 36, DOI: 10.1186/s12986-025-00924-1.

10 P. Zhang and M. X. Wu, A clinical review of phototherapy for psoriasis, *Lasers Med. Sci.*, 2018, **33**(1), 173–180, DOI: 10.1007/s10103-017-2360-1.

11 P. P. Mokoena, I. M. Nagpure, V. Kumar, R. E. Kroon, E. J. Olivier, J. H. Neethling, H. C. Swart and O. M. Ntwaeaborwa, Enhanced UVB emission and analysis of chemical states of $Ca_5(PO_4)_3OH$:Gd^{3+},Pr^{3+} phosphor prepared by co-precipitation, *J. Phys. Chem. Solids*, 2014, **75**(8), 998–1003, DOI: 10.1016/j.jpcs.2014.04.015.

12 M. Misiak, O. Pavlosiuk, M. Szalkowski, A. Kotulska, K. Ledwa and A. Bednarkiewicz, On the role of Gd^{3+} ions in enhancement of UV emission from Yb^{3+}–Tm^{3+} up-converting LiYF4 nanocrystals, *Nanotechnology*, 2023, **34**, 345702, DOI: 10.1088/1361-6528/acd701.

13 L. Reddy, Exploring Gd^{3+}-activated calcium-based host materials for phototherapy lamps: A comprehensive review, *Heliyon*, 2024, **10**, e34477, DOI: 10.1016/j.heliyon.2024.e34477.

14 A. O. Chauhan, *Borate Phosphor for Phototherapy Application*, CRC Press, Taylor & Francis Group, 2022, 1st edn, (eBook ISBN 9781003207757), DOI: 10.1201/9781003207757.

15 T. Nonami and S. Tsutsumi, Study of diopside ceramics for biomaterials, *J. Mater. Sci.: Mater. Med.*, 1999, **10**, 475–479, DOI: 10.1023/A:1008996908797.

16 P. Zadehnajar, M. H. Mirmusavi, S. Soleymani Eil Bakhtiari, H. R. Bakhsheshi-Rad, S. Karbasi, S. RamaKrishna and F. Berto, Recent advances on akermanite calcium-silicate ceramic for biomedical applications, *Int. J. Appl. Ceram. Technol.*, 2021, **18**, 1901–1920, DOI: 10.1111/ijac.13814.

17 L. Jiang, C. Chang and D. Mao, Luminescent properties of $CaMgSi_2O_6$ and $Ca_2MgSi_2O_7$ phosphors activated by Eu^{2+}, Dy^{3+}, and Nd^{3+}, *J. Alloys Compd.*, 2003, **360**(1–2), 193–197, DOI: 10.1016/S0925-8388(03)00361-X.

18 L. Jiang, C. Chang, D. Mao and C. Feng, Luminescent properties of $CaMgSi_2O_6$-based phosphors co-doped with different rare earth ions, *J. Alloys Compd.*, 2004, **377**, 211–215, DOI: 10.1016/j.jallcom.2004.01.024.

19 Y.-H. Kim, L. Chung, M. Murli and H. Manghnani, High-pressure phase transformations in a natural crystalline diopside and a synthetic $CaMgSi_2O_6$ glass, *Phys. Earth Planet. Inter.*, 1994, **83**(1), 67–79, DOI: 10.1016/0031-9201(94)90112-0.

20 T. Maldiney, A. Bessière, J. Seguin, B. Viana, C. Richard and D. Scherman, Effect of core diameter, surface coating, and PEG chain length on the biodistribution of persistent luminescence nanoparticles in mice, *ACS Nano*, 2011, **5**(2), 854–862, DOI: 10.1021/nn101937h.

21 C. Wu and J. Chang, A review of bioactive silicate ceramics, *Biomed. Mater.*, 2013, **8**(3), 032001, DOI: 10.1088/1748-6041/8/3/032001.

22 I. E. Kolesnikov, A. A. Vidyakina, M. S. Vasileva, V. G. Nosov, N. A. Bogachev, V. B. Sosnovsky, M. Y. Skripkin, I. I. Tumkin, E. Lähderanta and A. S. Mereshchenko, The effect of Eu^{3+} and Gd^{3+} co-doping on the morphology and luminescence of NaYF4:Eu^{3+}, Gd^{3+} phosphors, *New J. Chem.*, 2021, **45**, 10599–10607, DOI: 10.1039/D1NJ02193A.

23 S. Kumar and P. D. Sahare, Gd^{3+} incorporated ZnO nanoparticles: A versatile material, *Mater. Res. Bull.*, 2014, **51**, 217–223, DOI: 10.1016/j.materresbull.2013.12.031.

24 V. Dubey, S. Agarwal and J. Kaur Mishra, Photoluminescence and thermoluminescence behavior of Gd-doped Y_2O_3 phosphor, *Optik*, 2014, **126**, 1–5, DOI: 10.1016/j.ijleo.2014.06.175.

25 H. Hejin Park., Modification of SnO_2 Electron Transport Layer in Perovskite Solar Cells, *Nanomaterials*, 2022, **12**(23), 4326, DOI: 10.3390/nano12234326.

26 K. R. Stein, D. J. Pearce and S. R. Feldman, Targeted UV therapy in the treatment of psoriasis, *J. Dermotol. Treat.*, 2008, **19**, 141–145, DOI: 10.1080/09546630701593465.

27 N. Hu, L. Lin, J. Tan, W. Wang, L. Lei, H. Fan, J. Wang, P. Müller-Buschbaum and Q. Zhong, Wearable Bracelet Monitoring the Solar Ultraviolet Radiation for Skin Health Based on Hybrid IPN Hydrogels, *ACS Appl. Mater. Interfaces*, 2020, **12**, 56480–56490, DOI: 10.1021/acsami.0c17628.

28 T. Gambichler, F. Breuckmann, S. Boms, P. Altmeyer and A. Kreuter, Narrowband UVB phototherapy in skin conditions beyond psoriasis, *J. Am. Acad. Dermatol.*, 2005, **52**, 660–670, DOI: 10.1016/j.jaad.2004.08.047.

29 R. C. Ropp, *Luminescence and the Solid State*, Elsevier Science, 2nd edn, 2004, vol. 21, Hardback ISBN: 9780444516619.

30 J. Han, Y. Yang, Y. N. Hu, X. Huang, Y. Lin, Q. Han, X. Liu and C. Wang, Exploring the structural stability and optical properties of rare-earth doped $K_3LuSi_2O_7$ phosphor from first-principles calculations, *J. Lumin.*, 2022, **251**, 119224, DOI: 10.1016/j.jlumin.2022.119224.

31 Q. Shi, F. You, S. Huang, H. Peng, Y. Huang and Y. Tao, Excited state dynamics of Gd^{3+} and energy transfer efficiency from Gd^{3+} to Tb^{3+} in (La, Gd)PO_4:Tb^{3+}, *J. Lumin.*, 2014, **152**, 138–141, DOI: 10.1016/j.jlumin.2014.01.064.

32 S. Prabhakar Dhale, N. S. Ugemuge, V. Singh, R. V. Barde and S. V. Moharil, Wet-chemical synthesis of 'snow stone' chiolite $Na_5Al_3F_{14}$:Ce^{3+},Gd^{3+} UVB emitting phosphors, *J. Mol. Struct.*, 2025, **1320**, 139533, DOI: 10.1016/j.molstruc.2024.139533.

33 O. Belahssen, H. Ben Temam, S. Lakel, B. Benhaoua, S. Benramache and S. Gareh, Effect of optical gap energy on the Urbach energy in the undoped ZnO thin films, *Optik*, 2015, **126**, 1487–1490, DOI: 10.1016/j.ijleo.2015.04.010.

34 P. Pust, P. J. Schmidt and W. Schnick, A revolution in lighting, *Nat. Mater.*, 2015, **14**, 454–458, DOI: 10.1038/nmat4270.

35 M. Tammer, G. Sokrates: Infrared and Raman characteristic group frequencies: tables and charts, *Colloid Polym. Sci.*, 2004, **283**, 235, DOI: 10.1007/s00396-004-1164-6.

36 P. Pradhan, K. Singh, P. Saradhi Maram and S. Vaidyanathan, Oxide-Based Red Emitting Phosphors with High Color Purity and Their Versatile Applications: Synthesis, Structure, and Luminescence Properties, *ACS Appl. Opt. Mater.*, 2022, **1**, 132–146, DOI: 10.1021/acsaom.2c00022.

37 V. E. Hamilton, Thermal infrared emission spectroscopy of the pyroxene mineral series, *J. Geophys. Res.:Planets*, 2000, **105**, 9701–9716, DOI: 10.1029/1999JE001112.

38 K. Lebbou, *et al.*, Functional applications and luminescence properties of emission tunable phosphors $CaMoO_4$@-SiO_2:Ln^{3+} (Ln = Eu, Tb, Dy), *J. Alloys Compd.*, 2021, **857**, 157515, DOI: 10.1016/j.jallcom.2020.157515.

39 S. Dhale, N. S. Ugemuge, V. Singh, M. S. Shekhawat and S. V. Moharil, Moharil, Hydrothermal synthesis and luminescence of $NaCaYF_6$:Ln^{3+} (Ln^{3+} = Ce, Gd) synthetic gagarinite for UV applications, *Opt. Mater.*, 2024, **148**, 114888, DOI: 10.1016/j.optmat.2024.114888.

40 M. Saif, Luminescence based on energy transfer in silica doped with lanthanide titania ($Gd_2Ti_2O_7$:Ln^{3+}) [Ln^{3+} = Eu^{3+} or Dy^{3+}], *J. Photochem. Photobiol., A*, 2009, **205**, 145–150, DOI: 10.1016/j.jphotochem.2009.04.020.

41 A. Edgar, *Luminescent Materials*, Springer, Cham, 2017, DOI: 10.1007/978-3-319-48933-9_38.

42 L. Vijayalakshmi, K. Naveen Kumar and J. Dae Baek, Narrow-band UVB emission from non-cytotoxic Gd3+ -activated glasses for phototherapy lamps and UV-LED applications, *J. Mater. Sci.: Mater. Electron.*, 2022, **33**, 11938–11945, DOI: 10.1007/s10854-022-08156-2.

43 S. Liu, Y. Yan, X. Liu, Z. Cui, S. Jia, Y. Xing, S. Guo, B. Wang and Y. Wang., Concentration quenching inhibition and fluorescence enhancement in Eu3+ -doped molybdate red

phosphors with two-phase mixing, *RSC Adv.*, 2023, **13**(44), 31167–31175, DOI: **10.1039/d3ra05873e**.

44 M. Abraham, K. K. Thejas, A. K. Kunti, N. Amador-Mendez, R. Hernandez, J. Duras, K. G. Nishanth, S. K. Sahoo, M. Tchernycheva and S. Das, Strategically Developed Strong Red-Emitting Oxyfluoride Nanophosphors for Next-Generation Lighting Applications, *Adv. Opt. Mater.*, 2024, **12**(30), 2401356, DOI: **10.1002/adom.202401356**.

45 C. Sun, L. Lu, S. Wu, H. Sun and X. Mi, Photoluminescence properties and energy transfer mechanism of Eu^{3+}-Tb^{3+}-Pr^{3+} triple-doped Gd_2O_3 phosphors, *Ceram. Int.*, 2025, **51**, 20230–20238, DOI: **10.1016/j.ceramint.2025.02.188**.

46 J.-K. Lee, A. Ahmad Bhat, S. Watanabe, T. K. Gundu Rao and V. Singh, Unveiling the photoluminescence and electron paramagnetic resonance of Gd^{3+}-Doped $CaYAl_3O_7$ phosphor emitting narrowband ultraviolet B radiation, *Ceram. Int.*, 2025, **51**, 10415–10422, DOI: **10.1016/j.ceramint.2024.12.474**.

47 S. P. Dhale, N. S. Ugemuge, V. S. Singh and S. V. Moharil, UVB-emitting phosphors based on singly and co-doped Ce^{3+}, Gd^{3+} in Li_4ZrF_8 phosphors, *Spectrochim. Acta, Part A*, 2025, **325**, 125050, DOI: **10.1016/j.saa.2024.125050**.

48 X. Shan, X. Lv, D. Chen, Y. Zhang, L. Huang and Y. Liang, Synergistic Integration of NB-UVB Persistent Luminescence and Concentration-Dependent Photochromism in a Phosphate Phosphor for Multifunctional Applications, *Adv. Opt. Mater.*, 2025, e01335, DOI: **10.1002/adom.202501335**.

49 A. O. Chauhan, C. B. Palan, R. B. Butley, C. C. Jadhao, G. T. Lamdhade, K. B. Raulkar and S. K. Omanwar, Structural and Spectroscopic Properties of Gd^{3+} doped $CaSO_4$ Phosphor for Phototherapy Application, *Int. J. Sci. Res. Sci. Technol.*, 2025, **4**(12), 343–346, DOI: **10.32628/IJSRST2512294**.

50 D. L. Dexter, A Theory of Sensitized Luminescence in Solids, *J. Chem. Phys.*, 1953, **21**, 836–850, DOI: **10.1063/1.1699044**.

51 L. G. Van Uitert, Characterization of Energy Transfer Interactions between Rare Earth Ions, *J. Electrochem. Soc.*, 1967, **114**, 1048–1053, DOI: **10.1149/1.2424184**.

52 N. Yang, Z. Zhang, L. Zou, J. Chen, H. Ni, P. Chen, J. Shi and Y. Tong, A novel red-emitting phosphor with an unusual concentration quenching effect for near-UV-based WLEDs, *Inorg. Chem. Front.*, 2022, **9**, 6358–6368, DOI: **10.1039/D2QI01982E**.

53 P. A. Nagpure and S. K. Omanwar, Synthesis and photoluminescence study of rare earth activated phosphor $Na_2La_2B_2O_7$, *J. Lumin.*, 2012, **132**, 2088–2091, DOI: **10.1016/j.jlumin.2012.03.068**.

54 R. J. Fleming, Activation energies and temperature-dependent frequency factors in thermally stimulated luminescence, *J. Phys. D: Appl. Phys.*, 1990, **23**, 950, DOI: **10.1088/0022-3727/23/7/031**.

55 M. M. Lanje, M. M. Yawalkar, J. S. Dahegaonkar and S. J. Dhoble, Enhancement of photoluminescence emission of Gd^{3+} activated borate phosphors for phototherapy lamps: A review, *J. Phys.: Conf. Ser.*, 2021, **1913**, 012031, DOI: **10.1088/1742-6596/1913/1/012031**.

56 Y. J. Li, S. Ye, C. H. Wang, X. M. Wang and Q. Y. Zhang, Temperature-dependent near-infrared emission of highly concentrated Cu^{2+} in $CaCuSi_4O_{10}$ phosphor, *J. Mater. Chem. C*, 2014, **2**, 10395–10402, DOI: **10.1039/c4tc01966k**.

57 M. Deng, Y. Liang, Y. Shi, J. Wang, J. Chen and Q. Liu, Ultraviolet photoluminescent materials from traditional ion-activated phosphors to emerging carbon dots and perovskites, *Mater. Sci. Eng., R*, 2024, **159**, 100803, DOI: **10.1016/j.mser.2024.100803**.

58 Aachal A. Sharma, M. Rakshita, Payal P. Pradhan, K. A. K. Durga Prasad, S. Mishra, K. Jayanthi and D. Haranath, Efficacy of photodynamic therapy using UVB radiation-emitting novel phosphor material for non-surgical treatment of psoriasis, *J. Mater. Res.*, 2023, **38**(9), 2812–2822, DOI: **10.1557/s43578-023-01008-7**.

59 X. Wang, Y. Chen, P. A. Kner and Z. Pan, Gd^{3+}-activated narrowband ultraviolet-B persistent luminescence through persistent energy transfer, *Dalton Trans.*, 2021, **50**(10), 3499–3505, DOI: **10.1039/d1dt00120e**.

60 A. A. Sharma and D. Haranath, *Overview of Treating Skin Diseases and Rejuvenating Skin using Light Sources, Rare Earth – A tribute to the late Mr Rare Earth, Professor Karl Gschneidner*, Materials Research Forum LLC, 2024, vol. 164, pp. 143–176, DOI: **10.21741/9781644903056-3**.

61 F. Wu, H. Yang, Y. Zhu, G. Zhang and C. Pan, Design and Realization of a Flexible Wearable Non-Invasive Phototherapy Device, 2024 International Conference on Electrical Engineering and Photonics (EExPolytech), Saint Petersburg, Russian Federation, 2024, 27–30, DOI: **10.1109/EExPolytech62224.2024.10755593**.

62 R. Rendeiro, J. Jargus, J. Nedoma, R. Martinek and C. Marques, The possibilities of using a mixture of PDMS and phosphor in a wide range of industry applications, *Opto-Electron. Adv.*, 2024, **7**, 240133, DOI: **10.29026/oea.2024.240133**.

63 X. Yuan, J.-L. Zhou, L. Yuan, J. Fan, J. Yoon, X.-B. Zhang, X. Peng and W. Tan, Phototherapy: Progress, challenges, and opportunities, *Sci. China Chem.*, 2025, **68**, 826–865, DOI: **10.1007/s11426-024-2411-7**.

64 M. Li, C. Wang, Q. Yu, H. Chen, Y. Ma, L. Wei, M. X. Wu, M. Yao and M. Lu, A wearable and stretchable dual-wavelength LED device for home care of chronically infected wounds, *Nat. Commun.*, 2024, **15**, 9380, DOI: **10.1038/s41467-024-53579-6**.